

# Study of the Surface Morphology and Inclusions of Heavy Metals in Basal-Faceted Sapphire Ribbons Using In-Line X-Ray Phase-Contrast Imaging

T. S. Argunova<sup>a, \*</sup>, V. G. Kohn<sup>b</sup>, J.-H. Lim<sup>c</sup>, V. M. Krymov<sup>a</sup>, and A. V. Ankudinov<sup>a</sup>

<sup>a</sup> Ioffe Physical–Technical Institute, St. Petersburg, 194021 Russia

<sup>b</sup> National Research Centre “Kurchatov Institute”, Moscow, 123182 Russia

<sup>c</sup> Pohang Accelerator Laboratory, Pohang Light Source-II, Pohang, South Korea

\*e-mail: argunova@mail.ioffe.ru

Received June 19, 2024; revised July 31, 2024; accepted July 31, 2024

**Abstract**—This study presents the results of research concerning microsteps on the surface and the inclusions of heavy metals in the volume of sapphire ribbons grown using Stepanov’s method. Basal-faceted sapphire ribbons exhibit a low density of steps, which are caused by small changes in the orientation of the growth surface or the thickness of the ribbon. Phase contrast imaging using synchrotron radiation is employed to study the defects. It is shown for the first time that the height of a step of 1  $\mu\text{m}$  can be determined directly from the image. An analytical solution for the intensity distribution of the step in the case of fully coherent X-ray radiation is obtained. When the phase shift is small, there is a direct proportionality between contrast and step height, and the inverse problem is easily solved. The height obtained using the phase-contrast-imaging method is confirmed by measurements using atomic force microscopy. To analyze microinclusions, a computer simulation program is used, which allows for assessment of their sizes. We find that the experimental contrast matches the theoretical calculations only if the calculated intensity profile is convolved with a Gaussian function. The full width at half maximum of the Gaussian is independently obtained from preliminary measurements.

**Keywords:** sapphire, Stepanov’s method, microsteps, metal inclusions, synchrotron radiation, phase contrast, computer simulation

**DOI:** 10.1134/S1027451024701817

## INTRODUCTION

The properties of crystal surfaces play a central role in many natural and industrial processes. The key aspects of surface structure include defects in thin coatings, the thickness of lithographic reliefs, and the structure of faces. A critical condition for successful solution of the inverse problem of reconstructing the surface structure of single crystals is the ability of the research method to identify steps, terraces, vicinals, depressions, inclusions, pores, slits and microcracks. The formation of the growth surface occurs in complex environments that are inaccessible to solid-state probes with a high spatial resolution. Therefore, the morphology is studied after crystal growth using high-resolution optical and electron microscopy methods.

Phase-contrast microscopy in visible light may require coatings to enhance its sensitivity. Scanning electron microscopy studies, which cover the entire surface of the sample, are primarily qualitative. The application of transmission electron microscopy is limited to thin samples that are transparent to electrons. Only X-rays and neutrons possess a high pene-

tration capability and sensitivity to microscale and nanoscale reliefs.

Since X-ray radiation interacts weakly with matter, it has primarily been used to measure the spatially averaged distribution of the intensity. However, small-angle scattering and reflectometry allow for the acquisition of information about changes in the electron density within the irradiated portion of a small-sized material. Computer simulation of the intensity distribution provides insight into parameters such as surface roughness, amorphous layers, pores, particles, and so on. At the same time, a local change in the electron density, corresponding to a specific area in the sample, can be distinguished by a sharp change in the color of contrast in the X-ray image. A pixelated detector positioned in the nearly parallel beam of synchrotron radiation (SR) passing through the sample records information about the volume of the sample corresponding to each pixel, with the spatial resolution of the image being determined by the pixel size.

All X-ray imaging methods known in the previous century, such as radiography, diffraction topography,

and computed tomography, have benefited from the use of synchrotron radiation. The intense and coherent beams generated by third-generation SR sources have led to the development of new X-ray phase contrast methods based on interferometry, diffraction in crystals, in-line imaging [1], as well as coherent diffraction imaging and ptychography [2]. In particular, in in-line phase-contrast imaging (PCI), the beam from a SR source with a small angular size serves as an excellent probe, combining locality and coherence with a relatively large field of view. The application of this method for materials science has become standard practice, and the development of phase-contrast theory has defined the quantitative nature of the method [3]. At the same time, the computer simulation of phase-contrast images has developed in parallel, but independently. Specifically, the simulation of phase-contrast images allows for determination of the sizes of micro-objects within solid materials [4–6].

However, the potential of the PCI method for determining the surface morphology has not been sufficiently explored. This work presents, for the first time, the application of the PCI method to detect microsteps on the vicinal surface of single crystals. It can only be stated that similar studies are not known to us. Nevertheless, it is relevant to reference recent observations of hydrophobic plant surfaces [7, 8] or the top layer of low atomic number composites [9]. Unlike the qualitative results of these experiments, this work presents a quantitative analysis of the contrast of microsteps characteristic of basal-faceted sapphire ribbons [10]. Small changes in ribbon thickness or deviations of its surface from the singular face of the crystal lead to the formation of relatively sparse steps, making the ribbons an ideal model object for simulating phase-contrast images. Additionally, the ribbons contain inclusions of heavy metals [11, 12]. Interestingly, the phase-contrast image of sharp steps can be described by an analytical equation; however, to take into account the real conditions of the experiment, a computer program is still required. In this work, using image simulation, the height of microsteps on the growth relief is measured, and the size of microinclusions of tungsten and molybdenum in the sapphire matrix is determined.

## EXPERIMENTAL

Currently, the Pohang Light Source (PLS) in Pohang, South Korea, operates effectively with an electron energy of 3.0 GeV. The Synchrotron Radiation Center has two beamlines for obtaining phase-contrast images and diffraction topographs: BL6C and BL9D.

A feature of the BL9D station is the absence of optical elements between the bending magnet and the sample, except for two beryllium windows. Taking into account absorption in the sample, the crystalline absorber, and the beryllium windows leads to the for-

mation of a broad peak on the spectral curve, which is localized around 7–10 keV.

At the BL6C station, a wiggler with a stronger magnetic field compared to the bending magnet is used. An alternating field with an induction of 2.0 T is applied in the vertical direction, and the sinusoidal trajectory of the electron beam lies in the horizontal plane. The increase in radiation intensity from the wiggler is associated with larger transverse oscillations of the electrons and angular deviations from the propagation direction. These deviations significantly exceed the angle of natural collimation,  $\psi = mc^2/E_e$ , where  $m$  and  $E_e$  are the mass and energy of the electrons, respectively, and  $c$  is the speed of light, which in this case is approximately  $35''$ . The small bending radius of the trajectory expands the photon spectral range towards higher energies: 23–50 keV. Within this broad range, the monochromator selects a peak at a given energy in a narrow spectral region,  $\Delta E/E = 2.9 \times 10^{-4}$ , where  $E$  is the photon energy. The high thermal load on the first monochromator, located in the optical chamber 36 m from the SR source, is approximately 10 kW. To dissipate such a large amount of heat, cooling with liquid nitrogen is used. However, residual heat may cause bending of the lattice planes of the first monochromator [13].

Image visualization is based on the conversion of X-ray radiation into visible light. The luminescent image on the scintillation screen is projected by an optical lens onto a charge-coupled device (CCD) matrix. Each image element is converted into an electrical signal and stored in the computer's memory. The properties of the screen significantly affect the quality of the detector. The scintillator screens used, such as CsI, CdWO<sub>4</sub>, or YAG:Ce, have a high photon output and are virtually free of defects. However, the finite size of the CCD chip results in a limited field of view compared to X-ray films. Therefore, high-resolution X-ray films are used alongside detectors at both the BL6C and BL9D stations. Additionally, a field of view of several tens of micrometers squared is provided by panels produced using complementary metal–oxide–semiconductor (CMOS) technology.

Although the short-focus lens captures only a small portion of the light from the scintillator, and image clarity worsens with a wide aperture, the maximum resolution can only be achieved with the setup described above. Resolution is ensured by the small pixel size of the CCD chip, the high magnification of the lens, and the high quality of the screen. The detector used in this work was equipped with a PCO Edge CCD matrix (PCO, Germany). Each chip of this matrix had a resolution of  $2560 \times 2160$  pixels and a size of  $6.5 \times 6.5 \mu\text{m}$ . 16-bit analog-to-digital conversion was provided for each pixel. The optimized resolution with a  $20\times$  magnification lens was  $0.325 \mu\text{m}$ .

Accurate information about the parameters of the experimental setup is required for computer image

simulation. In this regard, we have optimized a previously proposed method for determining properties such as the transverse coherence length ( $l_{tc}$ ) and the effective transverse size of the synchrotron-radiation source ( $w_s$ ) [14, 15]. The method is based on analysis of the visibility of Fresnel interference fringes created by an object with well-known parameters. Specifically, such objects include optical fibers made of tungsten wire, onto which amorphous boron is applied. The interference pattern for ideal experimental conditions is obtained through computer simulation. A comparison of the calculated pattern with the intensity distribution on the detector allows for the evaluation of  $l_{tc}$  and  $w_s$ .

Unlike the previously used approach [14, 15], we consider the experimental intensity distribution as the result of the combined effects of various factors, rather than just the parameters  $l_{tc}$  and  $w_s$ . Non-smooth beryllium windows, distortions of the X-ray mirrors' shape, monochromator crystals with slight curvature of the Bragg planes, vibrations, etc., can cause a loss of coherence. In practice, the observed interference pattern is often obtained after calculating the convolution of the ideal pattern, theoretically calculated for a point source, with a Gaussian function with a certain half-width. The half-width of the Gaussian function is a parameter of the experimental setup as a whole. The value of this parameter, determined for specific experimental conditions, can be used when determining the sizes of characteristic features observed in samples.

Figure 1a shows the phase-contrast image of an optical fiber made of tungsten wire with a diameter of 15  $\mu\text{m}$ , onto which amorphous boron is applied. The total diameter of the fiber is 100  $\mu\text{m}$ . The detector is located at a distance of  $r_d = 10$  cm from the sample. The intensity distribution, measured across the image at the center of the frame, is presented in Fig. 1b. The calculation was performed using the XRWP (X-Ray Wave Propagation) software [16] with a Gaussian function half-width of zero. The calculated intensity distribution is presented in Fig. 1c. It is noticeable that the minimum in the experimental curve (Fig. 1b) is higher than in the theoretical curve (Fig. 1c). This indicates the presence of a parasitic background, which needs to be removed for correct comparison of the curves. However, the main difference is that the intensity oscillations of the image are smoothed. By adjusting the half-width of the Gaussian function, it was determined that the best match with the experimental data occurs when the half-width of the Gaussian function is 1.8. The result is shown in Fig. 1d. The simple convolution with the Gaussian function allowed for reproduction of the experimental pattern with rather high accuracy.

When the detector is placed at a distance of  $r_d = 20$  cm from the sample, the overall appearance of the pattern does not change, but the period of intensity oscillations in the image becomes larger. In this case, the best

match with the experimental curve is obtained with a Gaussian half-width of 2.0. Then, for a distance of  $r_d = 40$  cm, the best match is observed with a Gaussian half-width of 3.6. If the size of this parameter were determined only by the size of the source, then when the distance is doubled, it should also double. However, we did not observe this pattern. More precisely, the increase in the Gaussian half-width was determined by a factor that increased with distance, plus an additional factor. Thus, it can be concluded that in situations where all factors contributing to the loss of coherence are not fully known, the best match with the experiment is achieved by convolving the ideal curve with a Gaussian function. The Gaussian half-width is varied to find the value that leads to the best agreement between the calculated and experimental data. This approach works well in cases where the synchrotron-radiation beam, for some reason, changes its position in space relative to the detector with a period shorter than the measurement time, meaning it vibrates.

## RESULTS

In profiled sapphire crystals, there are volumetric defects that can be grouped under the general term "inclusions." These include not only gas-filled pores but also metal inclusions. The sizes of these defects range from less than 1  $\mu\text{m}$  to several tens of micrometers or more [11, 12]. The general condition for pore formation is supersaturation of the melt with dissolved gases. The sources of foreign solid-phase inclusions can be the crucible, shaper, and other elements of the technological equipment that contain molybdenum (Mo) and tungsten (W). At the melting temperature of sapphire, volatile oxides of molybdenum and tungsten enter the melt. The reduction of these oxides and the formation of microparticles occur through the intermediary of aluminum suboxides present in the melt. These microparticles of Mo and W are then captured by the crystallization front and form inclusions within the volume of the ribbons [11, 12]. Previous publications have shown that gas pores can become sources of dislocations. Results from the computer simulations of phase-contrast images have helped understand the role of the size and shape of micropores in plastic deformation processes [17]. At the same time, the contribution of foreign inclusions to the generation of structural defects remains unclear. A key advantage of the PCI method is the relatively large field of view on the sample, which is determined by the size of the synchrotron-radiation beam, not limited by optical elements. The experimenter can map the distribution of microinclusions and pores. However, it is important to remember that the actual size of a micro-object can only be obtained by determining the phase shift, as phase-contrast images are interference patterns.

Figure 2a shows a portion of the ribbon at the beginning of growth. In a region of approximately 0.2  $\text{mm}^2$ , numerous solid inclusions and thickness steps are

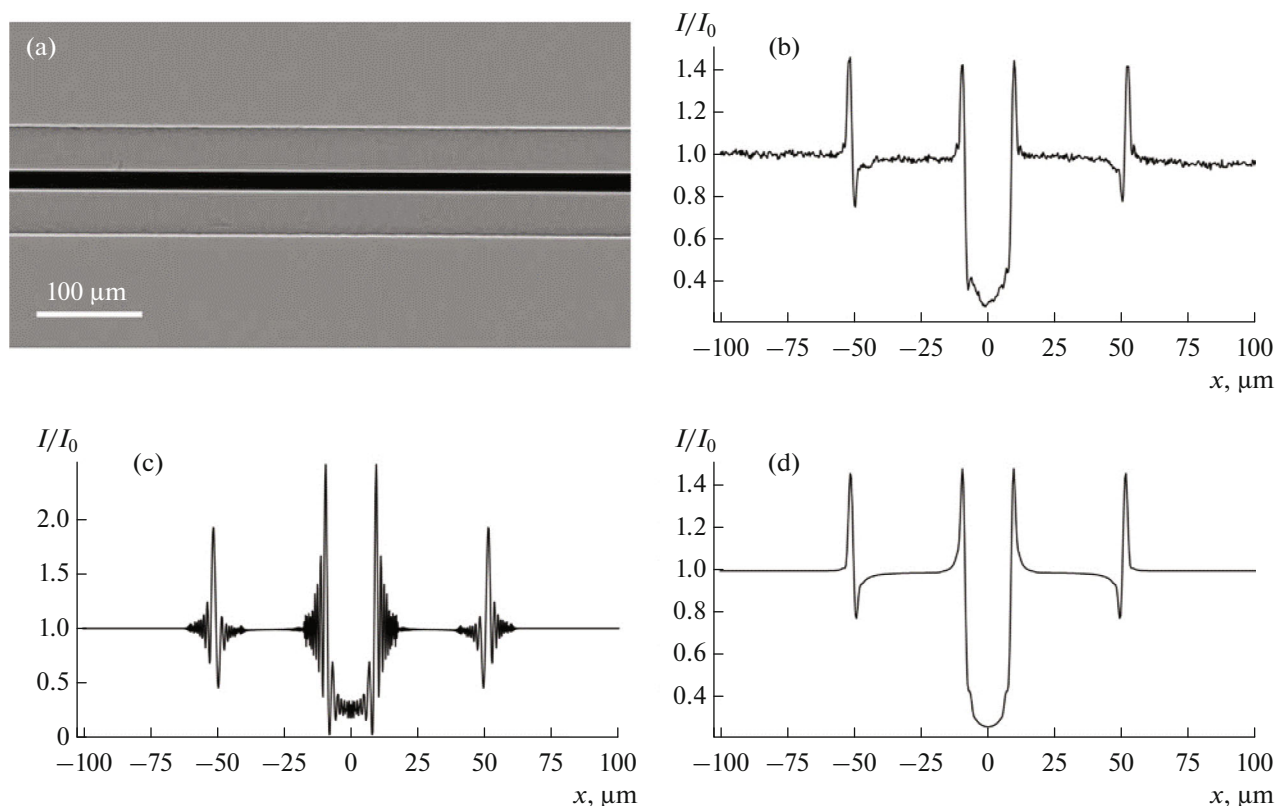


**Fig. 1.** (a) Phase-contrast image of an optical fiber. The source-to-sample and sample-to-detector distances are  $r_s = 36$  m and  $r_d = 10$  cm, respectively. (b) Experimental intensity distribution profile. (c) Theoretical profile constructed for a point source and ideal detector: the full width at half maximum of the Gaussian function is 0. A grid of 4096 points with a step size of  $0.25 \mu\text{m}$  was used for calculations. (d) Theoretical intensity profile of the image with a Gaussian full width at half maximum of  $1.8 \mu\text{m}$ .

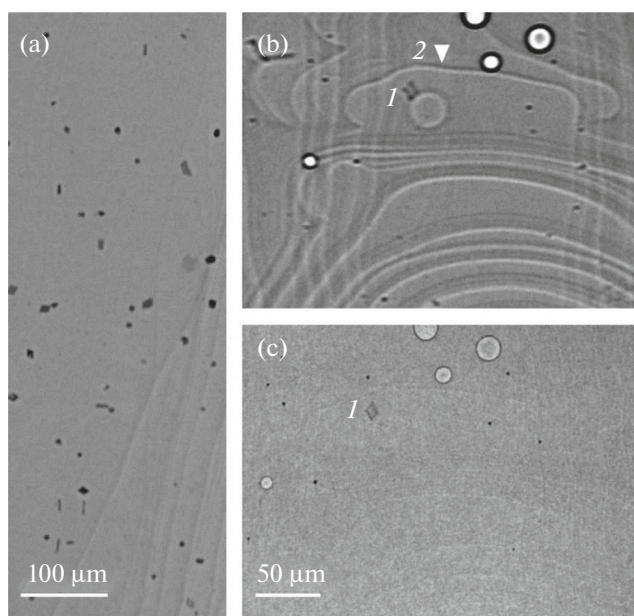


**Fig. 2.** Images of sections of sapphire ribbon: (a) Phase-contrast image of heavy metal inclusions at a sample-to-detector distance  $r_d = 15$  cm; (b) Steps, gas pores, and inclusions,  $r_d = 20$  cm. The metal inclusion (1) and step edge (2) are marked with numbers. (c) Image of the inclusion and step edge at  $r_d = 8$  mm.

observed. Unlike gas pores, which appear as black-and-white contrast figures in the images, metal inclusions of varying sizes appear as dark solid areas. In an optical microscope, only those inclusions close to the ribbon's surface are clearly visible. All these particles are also observed in the X-ray image. However, the smaller particles distributed throughout the sample volume rarely come into focus with the optical lens. In contrast, phase-contrast imaging reveals features of all inclusions, including those that are indistinguishable using optical microscopy. In the "hard" X-ray range, absorbing objects of microscopic size are not visible. The size limitation of the object can be overcome due to changing the phase.

Two phase-contrast images (Figs. 2b and 2c) differ in the sample-to-detector distance  $r_d$ . The surface relief of the ribbon appears bright and distinct (Fig. 2b) when  $r_d = 20$  cm. When  $r_d$  is shortened to 8 mm (Fig. 2c), the image of the relief dims and almost blends with the background of the image. The visibility of the step in thickness is determined by the brightness of its black-and-white contrast. If the intensity profile of the image, covering the maximum and its adjacent minimum, is well-formed, the height of the step edge can be calculated using an analytical

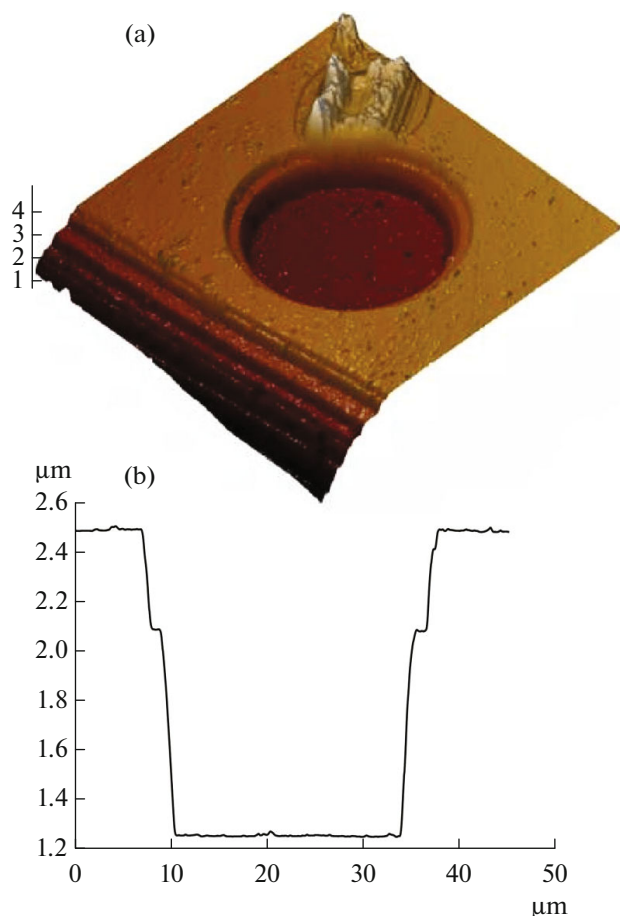


**Fig. 3.** (a) Image of a circular depression on the surface of sapphire ribbon obtained using an atomic force microscope. (b) Ribbon thickness along the line crossing the depression.

equation. However, when the value of  $r_d$  is several millimeters, the distances between oscillations in the first Fresnel zone do not exceed a submicrometer value. The interference pattern cannot be observed due to the detector's limited resolution.

In Figs. 2b and 2c, gas pores stand out. Their size is  $\geq 2r_1$ , where  $2r_1 = (\lambda r_d)^{1/2}$  is the diameter of the first Fresnel zone. The pores are visible due to the contrast of their edges. For the same reason, the contrast of a relatively large solid inclusion  $I$  changes little with the distance to the detector.

Near inclusion  $I$ , there is a closed circular boundary of some region (Fig. 2b). By the orientation of its black-and-white contrast, it can be immediately determined that this is a depression. The cause of depression formation on the surface of the ribbon can be explained by local overheating of the surface. Overheating is likely caused by the deposition of a hot metal particle at some distance from the crystallization front. Direct measurement of the relief height in this area of the sample was carried out using an Integra

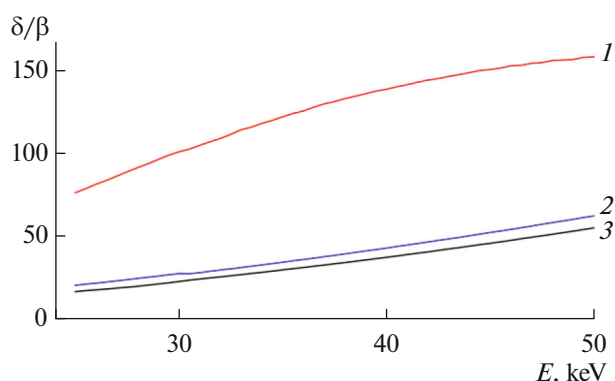


**Fig. 4.** Ratio of the decrement  $\delta$  of the refractive index of radiation  $n = 1 - \delta + i\beta$  to the absorption coefficient  $\beta$  for (1)  $\text{Al}_2\text{O}_3$  (shown with a coefficient of 0.1 for comparison), (2)  $\text{W}$ , and (3)  $\text{Mo}$ . The  $\delta/\beta$  ratio is a function that increases with the energy of X-ray radiation.

Aura atomic force microscope (NT-MDT, Russia). Figure 3 shows a 3D image of the sample relief (Fig. 3a) and a cross-sectional profile in the depression area (Fig. 3b). From the shape of the profile, it is concluded that the edges of the depression have the appearance of slightly inclined steps with a height of 1.24  $\mu\text{m}$ .

#### COMPUTER SIMULATION OF PHASE-CONTRAST IMAGES

The detection of heavy metal inclusions in the sapphire matrix is based on a comparison of absorption and refraction parameters. A feature of high-energy X-rays is that the decrement of the refractive index  $\delta$  significantly exceeds the absorption coefficient  $\beta$ . As shown in Fig. 4, in tungsten and molybdenum,  $\delta \approx 24\beta$  and  $\delta \approx 20\beta$ , respectively, while in sapphire,  $\delta \approx 90\beta$  at an X-ray energy of 20 keV. Therefore, when the absorption contrast is weak, the phase contrast inevitably reveals the presence of inclusions with micrometer or even submicrometer sizes.

In this study, a simplified model of a spherical particle is considered. Strictly speaking, inclusions can only be considered spherical when they are within the crystal volume and their shape remains unchanged under external influences. Although faceted inclusions form as a result of particle capture or phase separation [12], faceting was not taken into account in this model. Near the equator of the spherical particle, i.e., in the  $XZ$  plane (with the  $Z$  axis along the propagation of the SR beam and the  $X$  axis in one of the two perpendicular directions), the variation in thickness along the  $Y$  axis is rather small and can be neglected. In this case, it is sufficient to consider the one-dimensional intensity distribution only along the  $X$  axis. The calculation was performed using the XRWP software [16], in which wave propagation in free space is taken into account according to the Huygens–Fresnel principle,

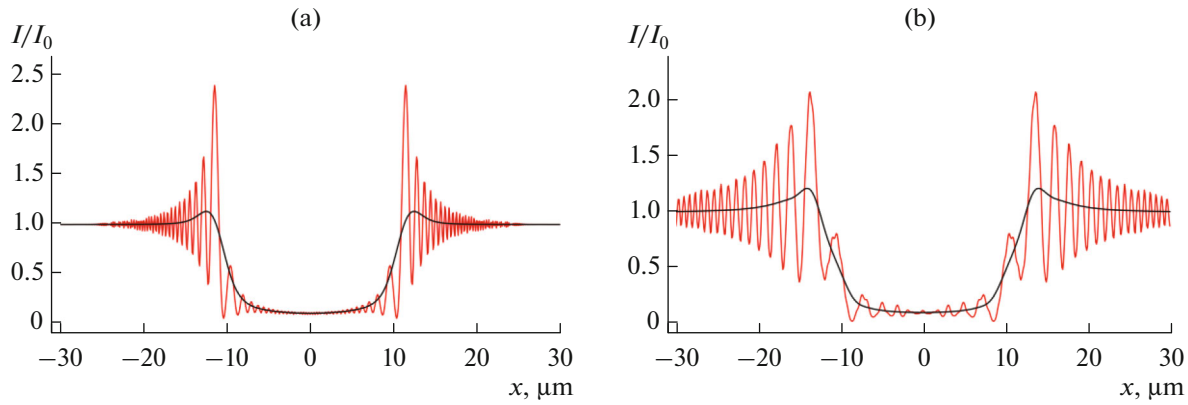


**Fig. 5.** Theoretical intensity profiles of the tungsten (W) inclusion in the sapphire ( $\text{Al}_2\text{O}_3$ ) matrix at  $r_d =$  (a) 5 and (b) 20 cm, obtained (red curve) for a point SR source and ideal detector and (black curve) as a result of convolution with a Gaussian function, when the Gaussian half width is  $3 \mu\text{m}$ .

as the convolution of the SR wave function with the Fresnel propagator. In this approach, the Fourier transform is applied, and calculation is carried out using the fast Fourier transform (FFT) method [18].

The calculated intensity profiles of X-ray images of a tungsten inclusion in a sapphire matrix are shown in Fig. 5 for sample-to-detector distances of 5 and 20 cm. The inclusion diameter is taken as  $20 \mu\text{m}$ . The graphs show only the central part of the calculated area, which is  $60 \mu\text{m}$  in size. The intensity in the inclusion region is almost zero. This means that even at a high photon energy of 20 keV ( $\lambda = 0.062 \text{ nm}$ ), tungsten absorbs X-ray radiation almost completely. The red curves in Fig. 5 represent the results of calculations made for a point SR source and an ideal detector. The black curves represent the result of the convolution with a Gaussian function (the full width at half maximum of the Gaussian function is  $3 \mu\text{m}$ ). Small oscillations of the phase contrast, clearly visible on the red curve, disappear on the black curve. Thus, the averaged image is determined solely by absorption. The transverse size of the inclusion can be accurately estimated by measuring the distance between the edges of the sharp intensity drop. As the sample-to-detector distance ( $r_d$ ) increases from 5 to 20 cm, the edges become less sharp after averaging due to an increase in the size of the Fresnel zones.

Now let us examine the step on the surface of the sapphire ribbon. The image of the step (2 in Fig. 2b) exhibits a characteristic black-and-white contrast, with the step height discernible solely through this contrast. Careful measurement of the contrast represents the most critical procedure when comparing the experimental and calculated intensity profiles. Images were recorded using a CCD matrix and saved in TIFF format, 16-bit with a range of values from 0 to 65536. During data processing, TIFF files were converted into matrices of numbers, from which fragments intended for analysis were cropped. Image anal-

ysis was performed using newly generated PNG files derived from the matrices. Intensity profiles were recorded along lines perpendicular to the selected segment of the step image. This procedure helps ensure accurate measurements of the step's height by comparing experimental and theoretical intensity profiles.

In particular, the experimental intensity distribution across step 2 (Fig. 1b) is shown by the black curve in Fig. 6. The deviations of the minimum and maximum intensity from the average value are approximately the same, which aligns with the theory of phase-contrast imaging for steps on the surface. It can be demonstrated that if the phase shift of the wave  $\phi \ll 1$ , the relative intensity of such an image in parallel and monochromatic radiation is described by the following function:

$$\begin{aligned} I/I_0 &= 1 + \phi [S(x/x_0) - C(x/x_0)], \\ \phi &= K\delta t, \quad x_0 = (\lambda r_d/2)^{1/2}. \end{aligned} \quad (1)$$

Here,  $S(x)$  and  $C(x)$  are the Fresnel integrals, sine and cosine respectively;  $r_d$  is the distance from the object to the detector;  $\phi$  is the phase shift of the wave on the step. The calculated intensity, derived from Eq. (1), contains numerous oscillations. However, the experimental intensity profiles do not exhibit fine details. As a result of the convolving function (1) with a Gaussian function having a half-width of  $3 \mu\text{m}$ , a smoothed profile was obtained, shown by the red curve in Fig. 6. The contrast value, determined from the profile, is  $0.2\phi$ . Using the phase value  $\phi = 0.2$ , obtained by comparing the calculated contrast with the experimental one, and the tabulated value of  $\delta = 1.532 \times 10^{-6}$ , the step height  $t$  is determined from Eq. (1) by simple calculation;  $t = 1.12 \mu\text{m}$ . In Fig. 2, the circular depression and the step are separated by a distance of approximately  $20 \mu\text{m}$ . Considering that within these  $20 \mu\text{m}$  the surface of the ribbon is almost a smooth face, differing at a small angle from the singular one, the height of the adjacent steps can be considered nearly identi-

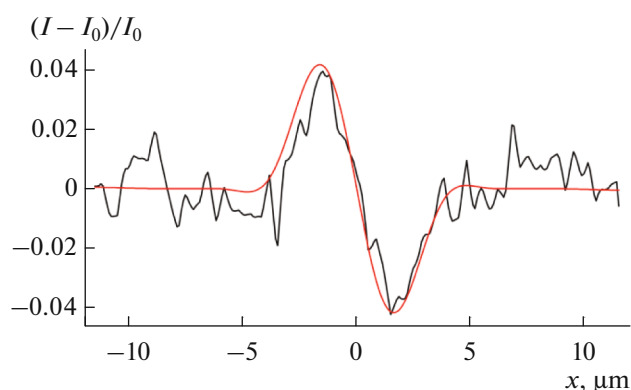


**Fig. 6.** (black curve) Experimental and (red curve) theoretical intensity profiles of the phase-contrast image of the step.

cal. Under this assumption, it can be concluded that the result of analysis using the PCI method corresponds to the result obtained through atomic force microscopy.

### CONCLUSIONS

The main result of this work is demonstration that the phase-contrast method allows for the accurate detection of changes in object thickness on the order of 1  $\mu\text{m}$  within the illumination area of the SR beam, even with a relatively large loss of beam coherence. As an example, the microrelief in the form of steps on the vicinal surface of a basal-faceted sapphire ribbon was studied. This result is obtained for the first time.

Comparing experimental results with theoretical calculations is a crucial condition of this work. The theoretical intensity profile for fully coherent radiation can be calculated as a power series based on the phase jump  $\phi$  created by the step since this jump is significantly smaller than unity. As a result, the image contrast is proportional to  $\phi$ , and the contrast profile can be calculated analytically. The consideration of coherence loss was carried out by calculating the convolution of the coherent image contrast with a Gaussian function, the half-width of which is known from preliminary measurements. The obtained step-height value has been confirmed by atomic force microscopy.

The study also investigates inclusions of heavy metals within a sapphire ribbon. Comparing the experimental curves with the results of theoretical simulations helped to understand the nature of the contrast and determine the size of the inclusions. For tungsten particles with a size of approximately 10  $\mu\text{m}$ , the standard absorption contrast provides the primary contribution to the image. The phase contrast is averaged under conditions of weak coherence of the SR beam.

The advantages of the method based on phase-contrast measurements include the simplicity of the experimental setup and the ability to assess the sizes of

micro-objects with acceptable accuracy. The locality of measurements is combined with an expanded overall area, which is possible through movement of the sample relative to the detector.

### FUNDING

The work of T.S. Argunova was supported by the Ministry of Science and Higher Education of the Russian Federation (agreement no. 075-15-2021-1349). The work of V.G. Kohn was carried out within the framework of the state task of the National Research Centre “Kurchatov Institute.”

### CONFLICT OF INTEREST

The authors of this work declare that they have no conflicts of interest.

### REFERENCES

1. A. Snigirev, V. Kohn, I. Snigireva, and B. Lengeler, *Nature* **384**, 49 (1996).  
[www.doi.org/10.1038/384049a0](https://doi.org/10.1038/384049a0)
2. P. A. Prosekov, V. L. Nosik, and A. E. Blagov, *Crystallogr. Rep.* **66**, 867 (2021).  
[www.doi.org/10.1134/S106377452134006X](https://doi.org/10.1134/S106377452134006X)
3. Ch. Zuo, J. Li, J. Sun, Y. Fan, J. Zhang, L. Lu, R. Zhang, W. Wang, L. Huang, and Q. Chen, *Opt. Lasers Eng.* **135**, 106187 (2020).  
[www.doi.org/10.1016/j.optlaseng.2020.106187](https://doi.org/10.1016/j.optlaseng.2020.106187)
4. S. Zabler, H. Riesemeier, P. Fratzl, and P. Zaslansky, *Opt. Exp.* **14** (19), 8584 (2006).  
[www.doi.org/10.1364/OE.14.008584](https://doi.org/10.1364/OE.14.008584)
5. V. G. Kohn, T. S. Argunova, and J. H. Je, *Appl. Phys. Lett.* **91**, 171901 (2007).  
[www.doi.org/10.1063/1.2801355](https://doi.org/10.1063/1.2801355)
6. T. S. Argunova and V. G. Kohn, *Phys.-Usp.* **62** (6), 602 (2019).  
[www.doi.org/10.3367/UFNe.2018.06.038371](https://doi.org/10.3367/UFNe.2018.06.038371)
7. T. Lauridsen, K. Glavina, T. D. Colmer, A. Winkel, S. Irvine, K. Lefmann, R. Feidenhan'l, and O. Pedersen, *J. Struct. Biol.* **188** (1), 61 (2014).  
[www.doi.org/10.1016/j.jsb.2014.08.003](https://doi.org/10.1016/j.jsb.2014.08.003)
8. Zh. Hu, M. Sun, Lv. Min, L. Wang, J. Shi, T. Xiao, Y. Cao, J. Wang, and C. Fan, *NPG Asia Mater.* **8**, e306 (2016).  
[www.doi.org/10.1038/am.2016.122](https://doi.org/10.1038/am.2016.122)
9. J. D. Yeager, S. N. Luo, B. J. Jensen, K. Fezzaa, D. S. Montgomery, and D. E. Hooks, *Compos. A* **43** (6), 885 (2012).  
[www.doi.org/10.1016/j.compositesa.2012.01.013](https://doi.org/10.1016/j.compositesa.2012.01.013)
10. A. A. Asryan, S. N. Rossolenko, V. N. Kurlov, and V. M. Krymov, *Bull. Russ. Acad. Sci.: Phys.* **73** (10), 1333 (2009).  
[www.doi.org/10.3103/S1062873809100062](https://doi.org/10.3103/S1062873809100062)
11. A. V. Borodin, V. A. Borodin, V. E. Iskorostinskaya, T. A. Steriopolo, I. I. Khodos, and A. N. Nekrasov, *Izv. Vyssh. Uchebn. Zaved., Mater. Elektron. Tekhn., No. 2*, 29 (2010).

12. E. R. Dobrovinskaya, L. A. Lytvynov, and V. Pishchik, *Sapphire: Material, Manufacturing, Applications* (Springer Science + Business Media, 2009).  
[www.doi.org/10.1007/978-0-387-85695-7](https://doi.org/10.1007/978-0-387-85695-7)
13. M. Ando, N. Sunaguchi, D. Shimao, A. Pan, T. Yuasa, K. Mori, Y. Suzuki, G. Jin, J.-K. Kim, J.-H. Lim, S.-J. Seo, S. Ichihara, N. Ohura, and R. Gupta, *Phys. Med.* **32**, 1801 (2016).  
[www.doi.org/10.1016/j.ejimp.2016.11.103](https://doi.org/10.1016/j.ejimp.2016.11.103)
14. V. Kohn, I. Snigireva, and A. Snigirev, *Phys. Rev. Lett.* **85** (13), 2745 (2000).  
[www.doi.org/10.1103/PhysRevLett.85.2745](https://doi.org/10.1103/PhysRevLett.85.2745)
15. V. Kohn, I. Snigireva, and A. Snigirev, *Opt. Commun.* **198** (4–5), 293 (2001).  
[www.doi.org/10.1016/S0030-4018\(01\)01544-9](https://doi.org/10.1016/S0030-4018(01)01544-9)
16. V. G. Kohn, Computer program XRWP. <https://xray-optics.ucoz.ru/XR/xrwpe.htm> Accessed February 1, 2025.
17. T. S. Argunova, V. G. Kohn, J.-H. Lim, V. M. Krymov, and M. Yu. Gutkin, *Materials* **16**, 6589 (2023).  
[www.doi.org/10.3390/ma16196589](https://doi.org/10.3390/ma16196589)
18. J. W. Cooley and J. W. Tukey, *Math. Comp.* **19**, 297 (1965).

*Translated by O. Zhukova*

**Publisher’s Note.** Pleiades Publishing remains neutral with regard to jurisdictional claims in published maps and institutional affiliations. AI tools may have been used in the translation or editing of this article.